ADVANCED HEALTHCARE MATERIALS
www.advhealthmat.de

# Antitumor Cream: Transdermal Hydrogel Containing Liposome-Encapsulated Ruthenium Complex for Infrared-Controlled Multimodal Synergistic Therapy

*Yu-Fei Yan, Xue-Lian Li, Li-Zhen Zeng, Qishuai Liu, Zhongyan Cai, Yanrong Ren, Xiaoxia Ren,* and Feng Gao**

**A transdermal drug delivery cream, which is non-invasive and painless, containing a liposome-encapsulated Ru(II) complex (LipoRu) is created for the treatment of skin cancer. This formulation capitalizes on the synergistic antitumor effects of two-photon excited photodynamic therapy (PDT), photothermal therapy (PTT), and chemotherapy. LipoRu exhibits effective tumor accumulation, efficient cellular uptake, pH-sensitive and infrared-accelerated release, and dual localization to the nucleus and mitochondria. The released Ru(II) complexes within cells exert multiple antitumor mechanisms, such as DNA topoisomerase and RNA polymerase inhibition, Type I and II PDT, PTT, DNA photodamage, and apoptosis and ferroptosis induction. The biodistribution and therapeutic efficacy of LipoRu in vivo are systematically compared via three distinct administration routes: intratumoral injection, intravenous injection, and transdermal delivery through topical cream application. The positive therapeutic effects of the LipoRu cream fabricated here in subcutaneous tumor-bearing mice offer optimistic potential for the painless and non-invasive treatment of both early-stage and advanced skin cancers, as well as superficially located solid tumors.**

## 1. Introduction

Skin cancer is the most frequently identified malignancy in the US.[1] Invasive melanoma, though accounting for only 1% of skin cancer cases, is the primary cause of skin cancer fatalities.[1] In 2024, an estimated 100640 new melanoma cases and 8290 deaths are expected.[2] The treatment of melanoma is stage-dependent (**Figure 1a**), taking into account the genetic characteristics of the tumor and the overall health of the patient. The treatment for localized melanoma (Stages I and II) primarily consists of surgical excision with some healthy tissue. Sentinel lymph node biopsy is conducted on thicker melanomas to assess for metastasis, which may necessitate lymphadenectomy if regional nodes are impacted (Stage III). Advanced melanoma (Stage IV) involves distant metastasis, requiring targeted therapy (BRAF, MEK, and KIT inhibitors), immunotherapy (PD-1/PD-L1 and CTLA-4 inhibitors, Interleukin-2, and oncolytic virus), and radiation therapy for symptom relief and control.[3]

Drug injections, whether intravenous (i.v.) or intratumoral (i.t.), are inevitable in these treatments and cause pain and discomfort. Despite advancements in skin and superficial tissue excision surgeries, scarring remains a concern, particularly for individuals who are more likely to develop scars, which can affect their physical appearance. Non-invasive drug delivery technologies are especially noteworthy for treating skin cancer in comparison to other types of tumors. Topical creams and patches are widely used to treat skin ailments, including inflammation, eczema, warts, and acne. Patches offer controlled, sustained release and are suitable for long-term use, while ointments, creams, and gels provide flexible application, rapid absorption, and patient comfort, are beneficial for precise and customizable dosing, and minimize skin irritation from adhesives. Hence, we aim to innovate by developing a non-invasive and painless transdermal delivery cream for treating superficially located or subcutaneous tumors.

Coordination complexes exhibit excellent biocompatibility and biological activity.[4] Phototherapy with metal complexes has gained significant attention, leading to numerous advancements in photodynamic therapy (PDT), photothermal therapy (PTT), and photoactivated chemotherapy (PACT).[5] These complexes offer benefits such as enhanced light absorption, prolonged excited

Y.-F. Yan, X.-L. Li, L.-Z. Zeng, F. Gao
Key Laboratory of Medicinal Chemistry for Natural Resource
Ministry of Education
School of Pharmacy
Yunnan University
East Outer Ring Road, Kunming 650500, P. R. China
E-mail: gaofeng@ynu.edu.cn
Q. Liu, Z. Cai, Y. Ren, X. Ren
Animal Research and Resource Center
School of Life Sciences
Yunnan University
East Outer Ring Road, Kunming 650500, P. R. China
E-mail: renxiaoxia001@ynu.edu.cn

The ORCID identification number(s) for the author(s) of this article can be found under https://doi.org/10.1002/adhm.202403563

**DOI: 10.1002/adhm.202403563**

 

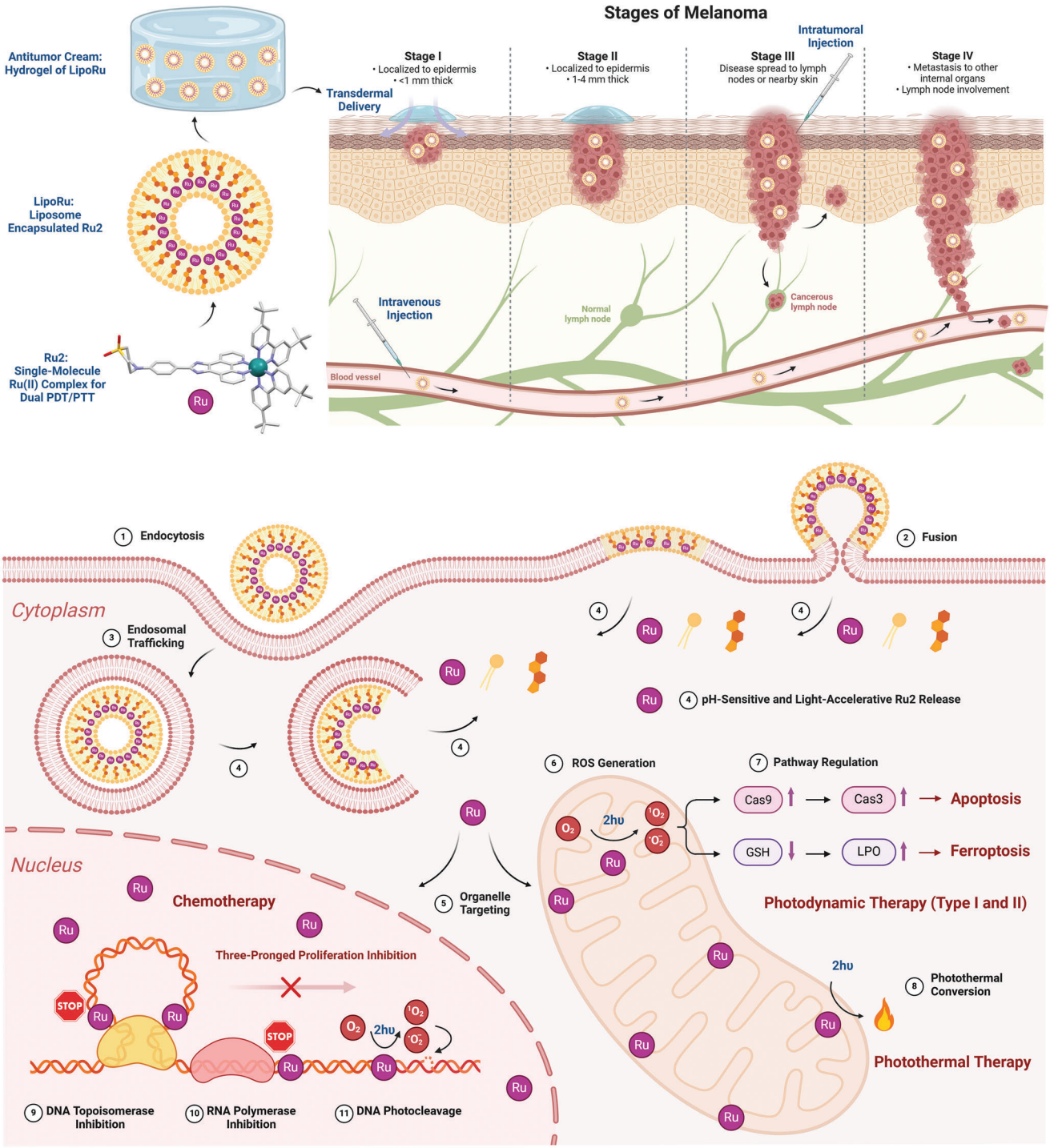


**Figure 1.** a) Single-molecule Ru(II) complexes designed in this study (represented by **Ru2**), liposome-encapsulated **Ru2** (**LipoRu**), antitumor cream fabricated from **LipoRu**, and different administration methods targeting the characteristics of melanoma at different stages. b) Mechanism of action of **LipoRu** for infrared two-photon photodynamic, photothermal, and chemotherapy through light-triggered $^1O_2$ and $O_2^{\bullet-}$ generation, apoptosis, ferroptosis, photothermal conversion, and three-pronged cell proliferation inhibition.

triplet state ($^3$ES) lifetimes, high quantum yields of emission and reactive oxygen species (ROS) generation, and structurally tunable physicochemical properties.[6] Large solid tumors often exhibit hypoxia, reducing the efficacy of oxygen-dependent PDT.[7] Oxygen-independent PTT can eradicate tumors via thermal ablation and increase intracellular oxygen pressure, thereby enhancing PDT.[8] Furthermore, ingenious designs have combined phototherapy with other therapies, such as sonodynamic and immunogenic therapy, yielding synergistic treatments that significantly improve efficacy and reduce the required dosage of therapeutic agents.[9]

Researchers have recently developed metal complexes for the multimodal synergistic treatment of melanoma.[10] A significant portion of these molecules is activated by infrared (IR) light, potentially overcoming the hinderance of melanin absorption in visible light PDT.[11] Intricately designed nanoparticles (NPs) encapsulating anti-tumor drugs can effectively accumulate in tumors through the enhanced permeability and retention (EPR) effect, exploiting tumor-specific features such as low pH and high hydrogen peroxide levels to facilitate the release or activation of drugs. Lipid nanoparticles (LNPs) represent a significant advancement in therapeutic delivery systems, exemplified by recently FDA-approved drugs. LNPs offer several advantages: enhanced drug stability, improved drug absorption and distribution by EPR effect, minimized systemic toxicity through drug encapsulation, controlled drug release, and reduced dosing frequency.[12] Their components, such as phospholipids and cholesterol, possess intrinsic high biocompatibility and low toxicity. Despite these benefits, current LNP drugs are primarily administered via injection, and their ability to effectively deliver drugs to the epidermis for skin cancer treatment remains unknown.

This study integrated above two innovative solutions: a non-invasive and painless antitumor cream for transdermal delivery and liposome-encapsulated antitumor therapeutic agents for targeted and efficient drug uptake by tumor. A series of Ru(II) complexes with multimodal synergistic antitumor effects were designed (Figure 1b) to increase the ROS production in hypoxic tumor environments and enhance the PCE, hence facilitating the synergistic effects of PDT and PTT by integrating 1,1-dioxidothiomorpholine (dotmp), a crucial moiety of Nifurtimox (an antiparasitic drug for Chagas disease), into Ru(II)-based PSs, as Nifurtimox was recently discovered to generate ROS under hypoxic conditions, thereby activating apoptotic pathways.[13] The versatile structure of dotmp also appears in the anti-inflammatory drug Filgotinib, the anti-HIV molecule GSK3640254, and the psychiatric disorder modulator Basmisanil.[14] The flexible six-membered heterocyclic structure of dotmp also has the potential to improve the photothermal conversion efficiency (PCE) of metal-based photosensitizers (PSs).[8d] The antitumor activity and mechanisms of the Ru(II) complexes were studied from photophysical, photochemical, and cell biology perspectives. The selected complex (**Ru2**) was further encapsulated into liposomes (**LipoRu**) without any solid particles and formulated into a topical cream using hydrogel. A systematic comparison of the biodistribution and therapeutic efficacy of **LipoRu** in vivo was conducted via three distinct administration routes: intratumoral injection, intravenous injection, and transdermal delivery through topical cream application. The transdermal cream demonstrated substantial therapeutic efficacy in subcutaneous tumor-bearing mice, highlighting the positive therapeutic effects of the **LipoRu** cream on both early-stage and advanced skin malignancies, as well as superficially situated solid tumors.

## 2. Results and Discussion

Three ancillary ligands have been used to construct **Ru1**−**3** (**Figure 2a**). The hydrophobic ancillary ligands tbubpy and dip have been shown to increase the bioavailability of Ru(II) complexes.[8e,f,15] The synthesis and characterization details, including $^1$H and $^{13}$C NMR spectra, HR-MS, IR spectra, and elemental analysis, are provided in the ESI (Figures S1–S6, Supporting Information).

The absorption and emission spectra of **Ru1**−**3** in aqueous solution are presented in Figure 2b, with key photophysical data summarized in **Table 1**. The absorbance followed the Beer-Lambert law (1−100 μM), indicating no aggregation. This was further supported by the Tyndall effect experiment (Figure S7, Supporting Information). The spectra of **Ru1**−**3** remained unchanged upon exposure to 450 nm LED or 808 nm laser irradiation in both aqueous solution (PBS buffer) and cell medium (Figures S8 and S9, Supporting Information), demonstrating excellent photostability. The absorption bands corresponding to the metal to ligand charge transfer (MLCT) were observed between 420 and 480 nm. The excited charge density plots of the photoexcited hole–electron pairs (Figure 2c for **Ru2** and Figures S10 and S11, Supporting Information, for **Ru1** and **Ru3**) for the most critical transitions ($f > 0.01$) and the simplified Jablonski diagraph (Figure 2d) showed that transitions ≈450 nm were predominantly attributed to MLCT from the $d_{metal}$ to the $\pi^*_{main}$ and intraligand (IL) transitions on the main ligand. Theoretical spectra (Figure 2e for **Ru2** and Figure S12, Supporting Information, for **Ru1** and **Ru3**) closely match the experimental data, showing the reliability of the computational results. **Ru1** and **Ru2** showed similar $\Phi_w$ values to $[Ru(bpy)_3]^{2+}$ (**Ru0**, 4.0%).[16] The primary $^1$ES transitions ($^*S_1$−$^*S_3$) for **Ru2** involve $^1$MLCT (main ligand) and $^1$MLCT+$^1$IL, whereas for **Ru1** and **Ru3**, they are $^3$MLCT (ancillary ligand) and $^1$MLCT+$^1$LLCT (ligand to ligand charge transfer). Moreover, the lowest three $^3$ES transitions ($T_1$−$T_3$) involve $^3$MLCT (ancillary ligand) for **Ru1** and **Ru3**, while for **Ru2**, the second $^3$ES ($T_2$) is a combination of $^3$MLCT (main ligand) and $^3$IL (main ligand). The presence of $^3$IL ES is advantageous for PSs.[17] Thus, **Ru2** may facilitate more efficient energy and electron transfer compared to **Ru1** and **Ru3**.

The curves and data for the two-photon absorption cross-section (TPACS) of **Ru1**−**3** were depicted in Figure 2f,g, and Table 1. The TPACS maxima vary from 376 to 401 GM (1 GM = $10^{-50}$ cm$^4$ s photon$^{-1}$), which exceeds those of most reported metal complexes at their respective TPA wavelengths.[6c,18] Specifically, at a wavelength of 808 nm, **Ru1**−**3** showed remarkably high TPACS values (286−305 GM), surpassing those of metal complexes known for their dual PDT/PTT activity.[8d–f] Consequently, it is anticipated that **Ru1**−**3** will exhibit potent PDT activity when exposed to 808 nm irradiation.

The quantum yields of $^1O_2$ and $O_2^{\bullet-}$ generation in aqueous solution ($\Phi_\Delta$) by **Ru1**−**3** were measured using ABDA and DHR123 assays (Figure 2h,i; Figures S13−S18, Supporting Information).

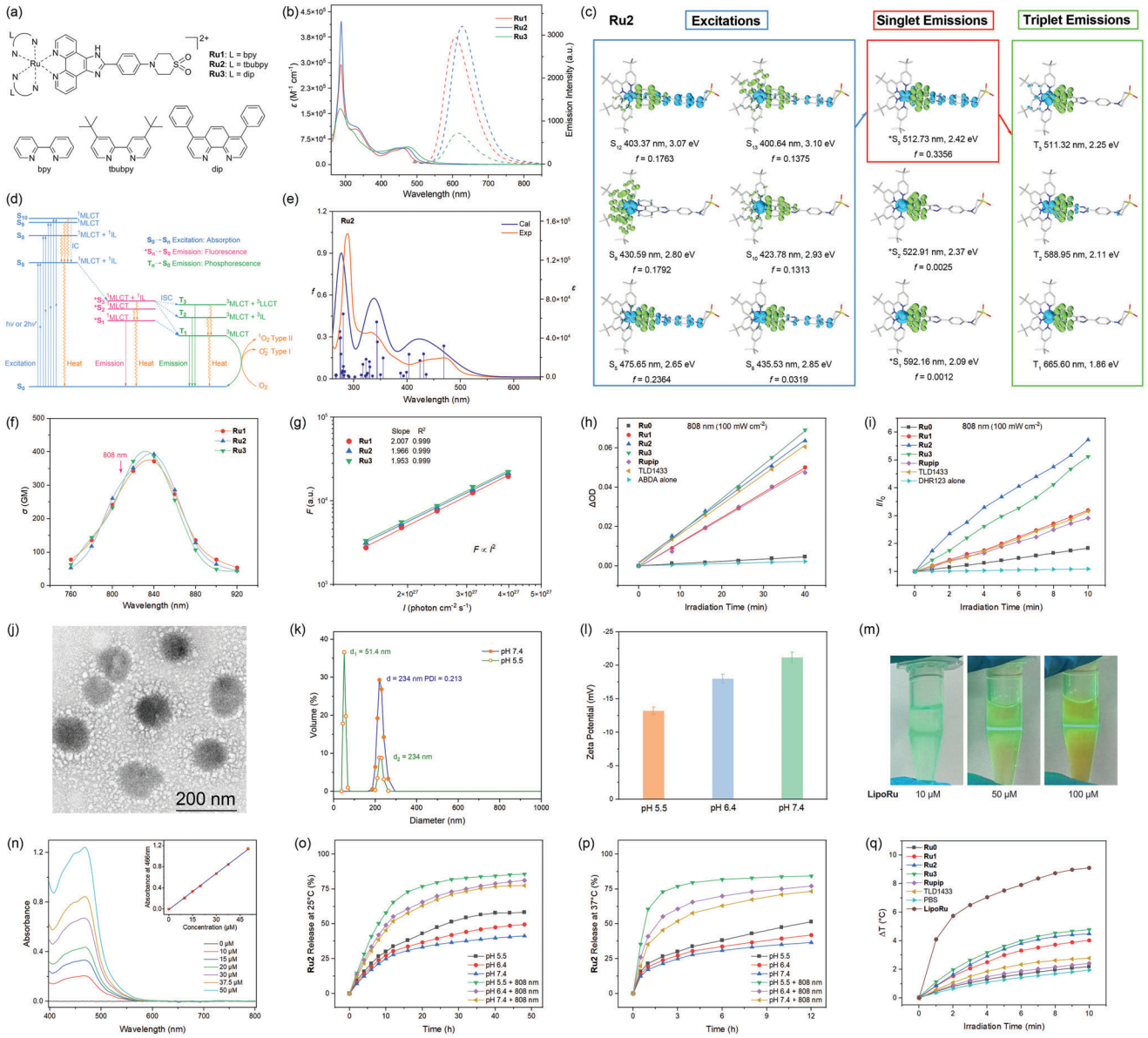


**Figure 2.** Photophysical and photochemical properties of Ru(II) complexes designed in this study (**Ru1**–**3**) and nanomaterial properties of liposome-encapsulated **Ru2** (**LipoRu**). a) Structure of **Ru1**–**3**. b) Absorption (solid) and emission spectra (dashed, excitation wavelength = 455 nm) of **Ru1**–**3** (10 μM) in aqueous solution. c) Real space representation of hole (blue) and electron (green) distributions of **Ru2** for the main excited state transitions responsible for excitation ($S_n$), singlet emission ($F_n$) and triplet emission ($T_n$). Excitation wavelength (nm), excitation energy (eV), and oscillator strength (*f*) for each hole-to-electron transition are presented. d) Simplified Jablonski diagram of **Ru2** for the energy transfer and main non-radiative decay (heat release) pathways. e) TDDFT (B3LYP/Lanl2DZ, CPCM for water) calculated absorption spectra and corresponding excited state transitions of **Ru2**. f) TPASCs ($\sigma$) of **Ru1**–**3** (50 μM in anhydrous THF solution) in the range of 760–920 nm. g) Linear fit of the logarithm plot of two-photon induced fluorescence intensity (*F*) versus the excitation intensity (*I*, at 820 nm). h) Singlet oxygen ($^1O_2$) generation rates represented by the OD decrease of ABDA versus irradiation time (min) in the absence and presence of **Ru1**–**3** by an 808 nm laser (100 mW cm$^{-2}$). $[Ru(bpy)_3]^{2+}$ (**Ru0**), $[Ru(bpy)_2(pip)]^{2+}$ (**Rupip**) and TLD1433 were tested as references. i) Superoxide anion ($O_2^{\bullet-}$) generation represented by the emission intensity increase ($I/I_0$) of DHR123 versus irradiation time (min) in the absence and presence of the tested Ru(II) complex by an 808 nm laser (100 mW cm$^{-2}$). j) Transmission electron microscope (TEM) images of **LipoRu**. k) Dynamic light scattering (DLS) analysis of particle size (diameter, pH 7.4 and 5.5) and polydispersity index (PDI) of **LipoRu** at pH 7.4. l) Zeta potentials of **LipoRu** in PBS solution under pH 5.5, 6.4, and 7.4. m) Tyndall effect experiment for 10, 50, and 100 μM of **LipoRu** in PBS solution. Concentrations represent **Ru2** in the PBS solution of the liposome. n) Calibration curve for measuring the concentration and encapsulation efficiency (EE) of **Ru2** in **LipoRu**. Release kinetics of **Ru2** for **LipoRu**, with or without 808 nm laser (100 mW cm$^{-2}$) irradiation, under pH 5.5, 6.4, and 7.7 at 25 °C (o) and 37 °C (p). q) Temperature rising curves of aqueous solutions of **Ru1**–**3** (100 μM in PBS) and **LipoRu** (50 μM for **Ru2**), as well as PBS, **Ru0** (100 μM), **Rupip** (100 μM), and TLD1433 (100 μM), irradiated by an 808 nm laser (100 mW cm$^{-2}$) for 10 min at 1-min intervals.

**Table 1.** Photophysical and photochemical data of **Ru1–3**.

| Complex | $\lambda_{abs}$/nm ($\epsilon \times 10^4$/M$^{-1}$ cm$^{-1}$])[a] | $\lambda_{em}$/nm[b] | $\Phi_w$/%[c] | $\sigma$/GM[d] | $\sigma_{808}$/GM[d] | $\Phi_{\Delta TP}(^1O_2)$/%[e] | $\Phi_{\Delta TP}(O_2^{\bullet-})$/%[e] | $\eta_{808}$/%[f] |
|---|---|---|---|---|---|---|---|---|
| **Ru1** | 460(4.78), 427(3.83), 327(10.5), 287(29.5) | 603 | 3.2 | 376 | 286 | 3.14 | 7.2 | 4.5 |
| **Ru2** | 469(4.91), 435(4.50), 332(11.0), 288(42.2) | 627 | 3.5 | 395 | 305 | 4.54 | 15.6 | 5.2 |
| **Ru3** | 475(5.24), 443(4.93), 319(9.87), 285(16.5) | 616 | 0.66 | 401 | 290 | 4.62 | 12.3 | 5.6 |

[a] Maximum absorption wavelength ($\lambda_{abs}$) and corresponding molar extinction coefficient ($\epsilon$) in aqueous solution; [b] Maximum emission wavelength ($\lambda_{em}$) in aqueous solution; [c] Photoluminescence quantum yield in aqueous solution ($\Phi_w$); [d] Two-photon absorption cross-section (TPSCS) at maximum MLCT absorption wavelength ($\sigma$) and 808 nm ($\sigma_{808}$); [e] Quantum yields of singlet oxygen and superoxide anion under 808 nm excitation ($\Phi_{\Delta TP}$) in aqueous solution; [f] Photothermal conversion efficiency (PCE) at 808 nm ($\eta_{808}$) in PBS solution.

**Ru1–3** exhibited exceptional $\Phi_\Delta$ values under both one-photon (OP, 450 nm LED, 50 mW cm$^{-2}$) and TP (808 nm laser, 100 mW cm$^{-2}$) irradiation, surpassing the values of **Ru0**, $[Ru(bpy)_2(pip)]^{2+}$ (**Rupip**), and TLD1433. These findings indicate that **Ru1–3** have considerable promise for a dual PDT mechanism, which involves both electron transfer (Type I) and energy transfer (Type II). The values of $\Phi_{\Delta TP}(^1O_2)$ and $\Phi_{\Delta TP}(O_2^{\bullet-})$ for **Ru1–3** under 808 nm irradiation were summarized in Table 1. **Ru2** exhibited the highest capability for generating ROS, which was attributed to its $^3$IL ES and high TPACS. Therefore, **Ru2** was selected for the preparation of LNPs and antitumor cream.

The liposome encapsulation of **Ru2** was performed by the thin film dispersion method (ESI). The measured apparent diameter of **LipoRu** was 150 ± 10 nm, as indicated by the transmission electron microscope (TEM, Figure 2j). The hydrodynamic diameter of **LipoRu** was 234 nm as determined by the dynamic light scattering (DLS, Figure 2k). The polydispersity index (PDI) of **LipoRu** at pH 7.4 was 0.213, indicating an excellent uniformity in particle size. When the pH value was adjusted to 5.5 and allowed for 24 h, 75% of **LipoRu** was observed to have a decreased size ($d_1$ = 51.4 nm), while the remaining 25% of **LipoRu** retained its previous size ($d_2$ = 234 nm). These findings indicate that **LipoRu** is stable at pH 7.4 but disassembles or releases its contents in the acidic environment of the tumor (pH 5.5). **LipoRu** demonstrated a negative and pH-dependent zeta potential (Figure 2l). The Tyndall effect assay conducted on **LipoRu** aqueous solution (Figure 2m) contrasted starkly with those of single molecule **Ru1–3** solutions (Figure S7, Supporting Information), hence verifying the formation of NPs. The absorbance of **Ru2** in the **LipoRu** solution adhered to the Beer-Lambert law (Figure 2n), suggesting a homogenous distribution within the system. The concentration of **Ru2** in the prepared **LipoRu** solution was determined to be 190 ± 9 μM, with an encapsulation efficiency (EE) of 92.3% (ESI).

The release kinetics of **LipoRu** were determined to depend on factors such as pH, temperature, and photoirradiation (Figure 2o,p). The release rate of **Ru2** was four times greater at 37 °C than at 25 °C. **LipoRu** released **Ru2** more effectively at the acidity level within tumor cells (pH 5.5) than in the tumor microenvironment (pH 6.4) and blood/normal cells (pH 7.4),[19] indicating a favorable accumulation and release of **Ru2** within tumor cells. Under 808 nm laser irradiation, the release rates of **Ru2** under various conditions increased significantly. It may be attributed to the photoexcited ROS, which cause oxidative degradation of the liposome membrane, or the photothermal effects that result in phase transition or membrane rupture.[20]

The photothermal conversion efficiency (PCE, $\eta_{808}$ in Table 1) was measured under 808 nm laser irradiation (Figure 2q; Figures S20–S22, Supporting Information). Complexes that contain a dip or tbubpy ancillary ligand have a wide range of rotation due to the phenyl and tbu groups, which can dissipate ES energy through a non-radiative energy pathway, resulting in a more remarkable PCE. As expected, **Ru2** and **Ru3** exhibited higher PCEs than **Ru1** without any rotatable group. The superior PCEs of **Ru1–3** in comparison to **Ru0**, **Rupip**, and **TLD1433** can be attributed to the favorable vibrational modes of the flexible six-membered heterocyclic structure of dotmp, which enables the more efficient dissipation of ES energy. The PCE of **LipoRu** was significantly higher than **Ru2**. Such enhancement in PCE can be attributed to the PS's dispersity in the liposomal membrane and its physical interaction with phospholipids.[20,21] The PCE improved by liposome encapsulation and the light-accelerated release of **Ru2** will be beneficial to the phototherapeutic effect of **LipoRu**.

The subcellular localization of **Ru2** and its liposome **LipoRu** in the A375 human melanoma cell line was initially investigated by confocal laser scanning microscopy (CLSM). After 15 min incubation of **Ru2** with the live adherent A375 cells in medium at 37 °C, almost all of **Ru2** was taken up by the cells. The fluorescence images of cells incubated with **Ru2** (**Figure 3a**) showed apparent colocalization with both the nuclear dye Hoechst33342 and the mitochondrial dye MitoTracker Green (MTG). For **LipoRu**, in addition to these two locations, **Ru2** was also observed near the cell periphery (Figure 3b). Bright-field images depicted the presence of a lipid layer enveloping the external cell membrane. This phenomenon may be attributed to the adherence or fusion of liposomes with the plasmic membrane. When the incubation time was increased to 60 min, no **Ru2** was observed at the membrane, indicating that **LipoRu** may penetrate A375 cells through membrane fusion (Figure 1b)[22] and the uptake of **LipoRu** via the membrane fusion could be accomplished within 60 min.

The cellular localization of **Ru1–3** and **LipoRu** in the nucleus and mitochondria was validated by ICP-MS (Figure 3c). The total uptakes of **Ru2** and **Ru3** were apparently greater than that of **Ru1**, due to their lipophilic nature (log *P*, **Table 2**), as revealed by the octanol/water partition assay (Figures S23 and S24, Supporting Information).[23] The uptake of **LipoRu** is 7 times greater than that of **Ru2**. This indicates that formulating **Ru2** into LNPs significantly enhances its cellular uptake. The data on the subcellular localization of the complexes were presented in Table 2. It can be inferred that **Ru1–3** target both nucleus and mitochondrion. Only ≈1% of the complexes were found in the cell membrane, indicating that the membrane was not their target. Although

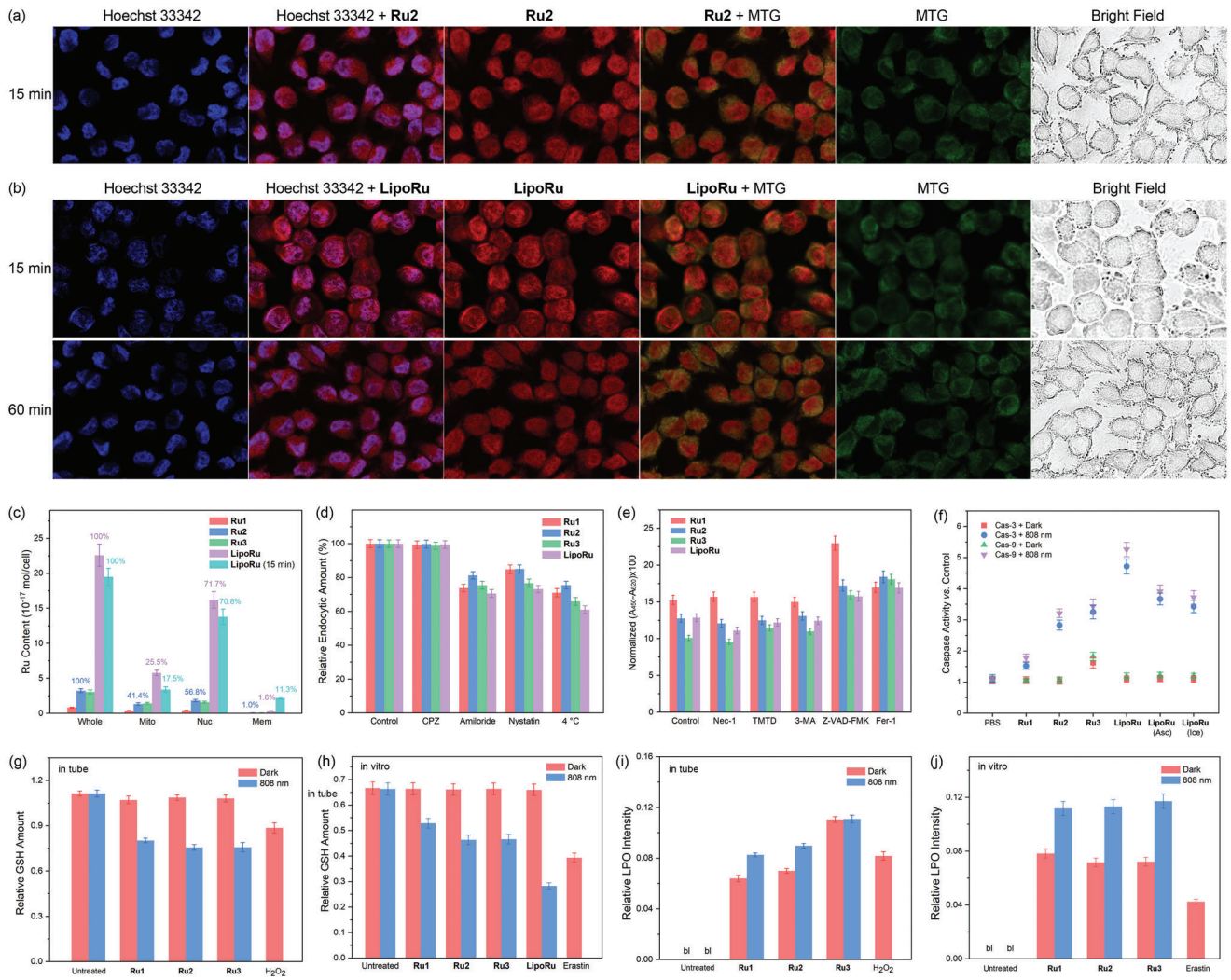


**Figure 3.** Cellular localization, uptake, endocytic mechanism, intracellular ROS production, and apoptosis- and ferroptosis-relative pathway regulation of **Ru1**–**3** and **LipoRu**. Subcellular colocalization of a) **Ru2** and b) **LipoRu** with Hoechst 33 324 and MitoTracker Green (MTG) in live adherent A375 cells by confocal laser scanning microscopy (CLSM). c) The amount of metal taken up by A375 cells determined by inductively coupled plasma mass spectrometry (ICP-MS). Whole: total uptake amounts by whole cell; Mito: mitochondria; Nuc: nuclei; Mem: membrane. The percentages indicate the appropriate proportions of each organelle's intake relative to the overall intake of the whole cell (mean, n = 3). d) Relative amounts of complexes **Ru1**–**3** in the presence of endocytic inhibitor chlorpromazine (CPZ, 10.0 μg mL$^{-1}$), amiloride (100.0 μg mL$^{-1}$), or nystatin (50.0 μg mL$^{-1}$) at 37 °C or without inhibitor at 4 °C taken up by A375 cells (n = 3). e) Normalized absorbance difference between 450 and 620 nm (× 100) in the presence of complex and inhibitors of different cell death mechanisms and irradiated by 808 nm laser determined by the CCK-8 assay (n = 3). Necrostatin-1 (Nec-1), tetraethylthiuram disulfide (TETD), 3-methyladenine (3-MA), benzyloxycarbonyl-Val-Ala-Asp (OMe) fluoromethylketone (Z-VAD-FMK), and ferrostatin-1 (Fer-1) were used as the inhibitors of necrosis, pyroptosis, autophagy, apoptosis, and ferroptosis, respectively. (f) Caspase-9 (Cas-9) and -3 (Cas-3) activity in A375 cells after treatment with PBS (control) and **Ru1**–**3** and **LipoRu** in the dark and under 808 nm laser (100 mW cm$^{-2}$) irradiation, as well as caspase activity in **LipoRu**-treated A375 cells under 808 nm (100 mW cm$^{-2}$) laser irradiation in the presence of ascorbic acid (Asc, 1.0 mM) and in an ice bath during irradiation (n = 3). Relative glutathione (GSH) amounts decreased by **Ru1**–**3** in the dark and under 808 nm (100 mW cm$^{-2}$) laser irradiation in cell-free aqueous solution (g) and A375 (h) cells (n = 3). Lipid peroxidation (LPO) induced by **Ru1**–**3** in the dark and under 808 nm (100 mW cm$^{-2}$) laser irradiation in cell-free aqueous solution (i) and A375 (j) cells (n = 3). $H_2O_2$ and Erastin were tested as the positive controls. bl: below the detection limit. $IC_{50}$ concentrations under TP excitation conditions were used for the complexes.

**LipoRu** exhibits a distribution ratio of 11.3% in the cell membrane after 15 min of incubation, the amount of **Ru2** remaining in the membrane decreased to just 1.6% when the incubation time was extended to 60 min. This aligns with the finding made by CLSM regarding the uptake mechanism of membrane fusion.

Endocytosis is also one of the primary uptake mechanisms for LNPs. **Ru1**–**3** and **LipoRu** exhibited decreased uptake in the presence of the macropinocytic pathway inhibitor amiloride or the caveolae formation inhibitor nystatin, or when the temperature was lowered to 4 °C (Figure 3d), suggesting that their uptake operated by both macropinocytosis and caveolae-mediated mechanisms energy-dependently. Tumors frequently encounter nutrient-limiting conditions and exhibit robust macropinocytosis, a mechanism that aids adaptation to nutrient deprivation by

**Table 2.** Biological data regarding DNA, enzyme, and cell of **Ru1**–**3**.

| Compound | log *P*[a] | $Ru_{Mito}$/%[b] | $Ru_{Nuc}$%[b] | $Ru_{Mem}$%[b] | $K_b/\times10^5$ $M^{-1}$[c] | $\Delta T_m$/°C[d] | $IC_{50\text{-}Topo}$/μM[e] | $IC_{50\text{-}RNAP}$/μM[f] | $IC_{50\text{-}PC}$/μM[g] |
|---|---|---|---|---|---|---|---|---|---|
| **Ru1** | −2.6 | 46 ± 5 | 50 ± 5 | 1.1 ± 0.2 | 23.2 ± 2.7 | 5.0 | 3.6 ± 0.2 | 0.36 ± 0.06 | 2.1 ± 0.2 |
| **Ru2** | 2.3 | 41 ± 5 | 57 ± 5 | 1.0 ± 0.2 | 9.05 ± 1.12 | 2.7 | 11.2 ± 0.4 | 0.42 ± 0.06 | 1.8 ± 0.2 |
| **Ru3** | 3.0 | 47 ± 4 | 53 ± 4 | 1.2 ± 0.2 | 18.1 ± 1.5 | 5.6 | 12.2 ± 0.4 | 0.32 ± 0.04 | 1.0 ± 0.1 |

[a] Apparent oil-water partition coefficients; [b] Distribution of **Ru1**–**3** in mitochondria (Mito), nuclei (Nuc), and membrane (Mem) of A375 cells detected by ICP-MS (mean ± SD, n = 3); [c] Binding constants of **Ru1**–**3** to CT-DNA; [d] Increases in CT-DNA melting points (denaturation temperatures) after complex-binding; [e] $IC_{50}$ for DNA topoisomerase inhibition; [f] $IC_{50}$ for RNA polymerase inhibition; [g] $IC_{50}$ for DNA photocleavage. $K_b$ and $IC_{50}$ were presented as value ± error.

internalizing extracellular proteins and necrotic cell debris. This process supports macromolecule synthesis and supplies energy to central carbon metabolic pathways. Ongoing endeavors are being undertaken to discover specific inhibitors of macropinocytosis for antitumor treatment.[24] The findings that **Ru1**–**3** and **LipoRu** enter tumor cells via the rare macropinocytic pathway may provide significant support in antitumor activity by leveraging the unique mechanisms of tumor cells to enhance the uptake of antitumor molecules or LNPs.

The nuclear targeting of **Ru1**–**3** may stem from their DNA affinity, allowing the complexes to participate in DNA-related chemotherapy and DNA photocleavage within the nucleus. As revealed by the spectroscopic titration (Figure S25, Supporting Information), binding constant ($K_b$) calculation, and DNA thermal denaturation experiment (Figure S26, Supporting Information), **Ru1**–**3** exhibited a moderate to high affinity for CT-DNA (Table 2), comparable to the reported pip-type Ru(II) complexes. DNA binders have the ability to impede the activity of RNA polymerase (RNAP) or DNA topoisomerase (Topo), enzymes responsible for synthesizing RNA from DNA templates in a process known as DNA transcription, or assist in the unwinding and coiling of DNA during replication and transcription, respectively. Topo and RNAP inhibitors can trigger cell death, particularly in rapidly dividing and proliferation cells, such as cancer cells, where fast DNA replication is necessary. **Ru1**–**3** exhibited remarkably higher inhibitory effects on both Topo and RNAP in comparison to many other inhibitors (Figures S27 and S28, Supporting Information; Table 2).[15,25] Therefore, **Ru1**–**3** act as substantial chemotherapeutic agents, in addition to their potent phototherapeutic properties. DNA-binding PSs can induce DNA cleavage by the produced ROS upon irradiation.[26] Figure S29 (Supporting Information) showed a gradual decrease in the quantity of supercoiled pBR322 DNA (Form I) following incubation with **Ru1**–**3** and exposure to the 808 nm laser. The $IC_{50}$ values in the micromolar range demonstrated their efficient DNA photocleavage activity, which could further boost their ability to directly kill and prevent the proliferation of tumor cells.

The cytotoxicity of **Ru1**–**3** toward A375 cells was tested by the CCK-8 assay (**Table 3**), both in the absence and presence of IR irradiation (808 nm laser, 100 mW $cm^{-2}$, light dose = 30.0 J $cm^{-2}$). **Ru1**–**3** displayed higher phototoxicity indexes (PI) than the clinically approved PDT drug 5-aminolevulinic acid (5-ALA). Cisplatin showed negligible phototoxicity (PI = 1.12). **Ru2** and **Ru3** with felicitous lipophilicity and optimal uptake exhibited remarkable PIs. The cytotoxicity decreased significantly when the irradiation was conducted in the presence of ascorbic acid (Asc, 1.0 mM) or in an ice bath, indicating a potent synergy between PDT and PTT with a combination index (CI) below 0.60 (CI < 0.7 implies a favorable synergistic effect).[27] The photocytotoxicity of tested compounds was marginally impacted when the cell plates were covered with commercial chicken breast skin during irradiation, assumably due to their outstanding TPACS and the high penetration of IR light.

The intracellular generation of ROS by **Ru1**–**3** was analyzed by flow cytometry. 2′,7′-Dichlorodihydrofluorescein diacetate (DCFH-DA) and Rosup were used as the detector and the positive control (Figure S30, Supporting Information). ROS were only detected in the presence of both a Ru(II) complex and light irradiation (808 nm laser). ROS scavenger Asc completely suppressed the production of photoinduced ROS, providing evidence for a PDT mechanism.

To explore the possible mechanisms of **Ru1**–**3** or **LipoRu**, the photocytotoxicity was further determined in the presence of inhibitors targeting several antitumor mechanisms. Necrostatin-1

**Table 3.** In vitro (photo)cytotoxicity ($IC_{50}$, μM) and PDT index (PI) of **Ru1**–**3**, **LipoRu**, 5-ALA, and cisplatin toward A375 human malignant melanoma upon two-photon excitation under various conditions.

| Complex | $IC_{50,Dark}$/μM[a] | $IC_{50,TP}$/μM[b] | PI[c] | $IC_{50,TP+Asc}$/μM[d] | $IC_{50,TP+Ice}$/μM[e] | $IC_{50,TP+Ice+Asc}$/μM[f] | CI[g] | $IC_{50,TP+CBS}$/μM[h] |
|---|---|---|---|---|---|---|---|---|
| **Ru1** | 62.6 ± 4.8 | 11.5 ± 1.0 | 5.44 | 18.6 ± 1.7 | 16.4 ± 1.6 | 65.7 ± 6.2 | 0.60 | 18.4 ± 1.6 |
| **Ru2** | 8.55 ± 0.76 | 0.143 ± 0.015 | 59.8 | 2.65 ± 0.27 | 1.583 ± 0.16 | 9.04 ± 0.86 | 0.52 | 0.207 ± 0.020 |
| **Ru3** | 2.47 ± 0.23 | 0.086 ± 0.011 | 28.7 | 1.04 ± 0.11 | 0.652 ± 0.068 | 4.06 ± 0.38 | 0.46 | 0.141 ± 0.012 |
| **LipoRu** | 6.72 ± 0.63 | 0.116 ± 0.010 | 57.9 | 1.63 ± 0.15 | 1.62 ± 0.18 | 6.87 ± 0.65 | 0.53 | 0.153 ± 0.016 |
| 5-ALA | 154 ± 13 | 84.5 ± 7.6 | 1.82 | 162 ± 15 | 106 ± 10 | 176 ± 17 | 2.1 | 165 ± 16 |
| Cisplatin | 2.14 ± 0.20 | 2.03 ± 0.19 | 1.12 | 2.26 ± 0.21 | 2.37 ± 0.22 | 2.19 ± 0.20 | 3.2 | 2.21 ± 0.20 |

[a] Under dark condition; [b] Upon two-photon excitation by an 808 nm laser (100 mW $cm^{-2}$, light dose = 30.0 J $cm^{-2}$); [c] Phototherapy index (PI) under TP excitation; [d] TP excitation in the presence of ascorbic acid (Asc, 1.0 mM); [e] TP excitation in an ice bath during irradiation; [f] TP excitation under both Asc (1.0 mM) and ice bath treatments; [h] Combination index; [g] TP excitation, and the cells were covered with chicken breast skin (1.5 mm in thickness). $IC_{50}$ was presented in mean ± SD (n = 3).

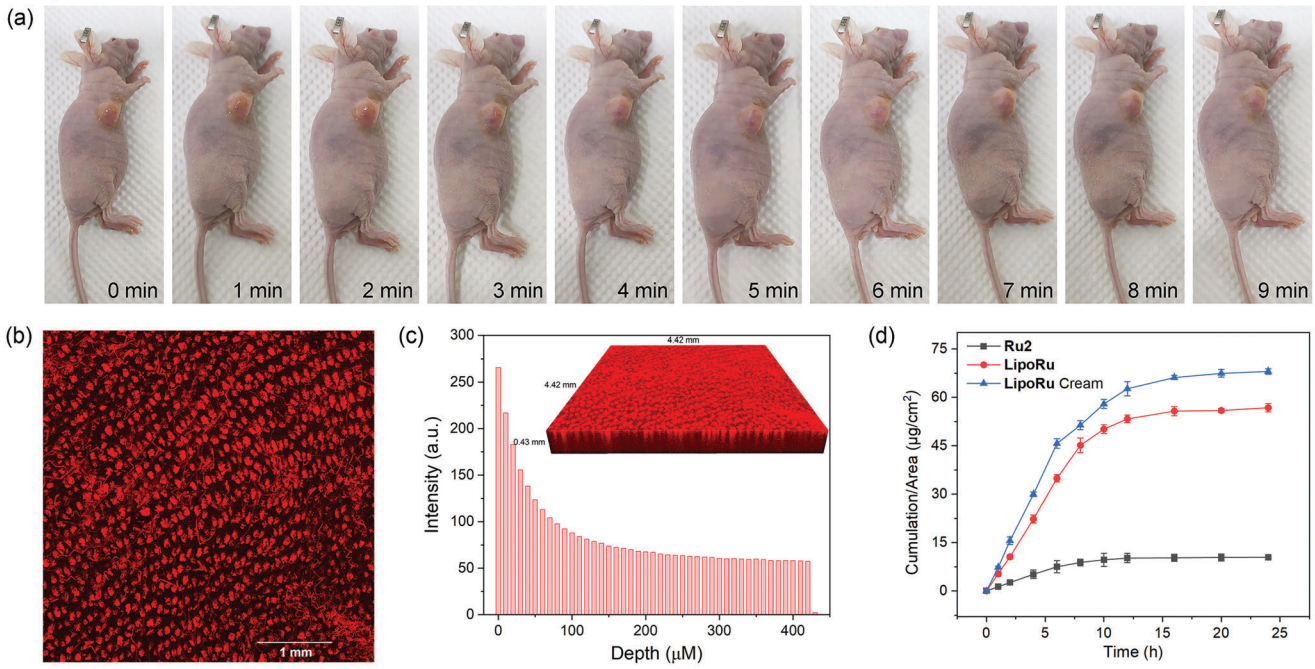


**Figure 4.** a) The absorption process of the topically applied **LipoRu** cream. b) Confocal imaging of nude mouse skin applied with 80 μL of **LipoRu** cream after 5 min. c) Fluorescence intensity of **Ru2** at different depths of skin (420 μm in thickness). Inset: Z-stack image of **Ru2** distributed within the whole depth of nude mice skin at 10 μm intervals. d) The amounts of **Ru2** that penetrated through the skin (mean ± SD, n = 3), measured using the Franz diffusion experiment for **LipoRu** cream and aqueous solutions of **Ru2** and **LipoRu**.

(Nec-1), tetraethylthiuram disulfide (TETD), 3-methyladenine (3-MA), benzyloxycarbonyl-Val-Ala-Asp fluoromethylketone (Z-VAD-FMK), and Ferrostatin-1 (Fer-1) were employed to inhibit necrosis, pyroptosis, autophagy, apoptosis, and ferroptosis, respectively. The antitumor mechanisms of **Ru1−3** or **LipoRu** toward A375 cells (irradiated by an 808 nm laser) were revealed to be apoptosis and ferroptosis, rather than other mechanisms (Figure 3e).

Caspase-9 (Cas-9) directly cleaves and activates caspase-3 (Cas-3) and caspase-7 to initiate cell death during apoptosis. The activity of Cas-9 and Cas-3 was quantified in the **Ru1−3** or **LipoRu**-treated A375 cells (Figure 3f). There was no activation of Cas-9 or Cas-3 in dark conditions, except **Ru3**, which aligns with its higher dark cytotoxicity. Upon irradiation, the caspase activity rose substantially while decreasing greatly either in the presence of Asc or when irradiated in an ice bath. This drop is due to the clearance of ROS or the suppression of heat generated via PTC. Apoptosis in complex-treated cells was further detected by flow cytometry, with paclitaxel serving as the positive control. **Ru1−3** clearly induced apoptosis of A375 cells when exposed to irradiation (Figure S31, Supporting Information). The ratios of apoptotic cells declined either in the presence of Asc or when exposed to irradiation in an ice bath, providing support for the photoinduction of apoptosis through a dual mechanism involving ROS and heat.

Ferroptosis is characterized as the increased oxidative stress in tumor cells caused by the generation of ROS and lowered levels of glutathione (GSH), which leads to the lipid peroxidation (LPO) of the membrane. The levels of GSH and LPO were investigated by both chemical and intracellular detections. **Ru1−3** and **LipoRu** apparently lowered the levels of GSH (Figure 3g,h) and increased the amounts of LPO (Figure 3i,j). These findings highlighted the process of ferroptosis.

As presented above, **Ru1−3** and **LipoRu** exhibit multimodal antitumor mechanisms, including PDT, PTT, chemotherapy, photoinduced apoptosis and ferroptosis, as well as direct DNA photocleavage. Significant synergistic effects between PDT and PTT have been revealed by the low values of CI. This experimental finding can be rationalized by the enhancement of tumor cell oxygenation through photothermal effect, which facilitates PDT. Additionally, the complexes and liposomes can exert chemotherapeutic effects by inhibiting DNA-related enzymes even in the absence of light. This positively contributes to the drug's activity in areas with insufficient irradiation, such as deeper-seated tumor regions.

To achieve transdermal drug delivery like creams or ointments, a hydrogel formulation containing **LipoRu** (**LipoRu** cream) was developed. The **LipoRu** cream exhibited excellent stability, as evidenced by the absence of any notable alterations in its appearance, viscosity (Figure S32, Supporting Information), and pH (Figure S33, Supporting Information) for a period of 30 days after its preparation. In order to verify the transdermal absorption performance of the cream, 80 μL of **LipoRu** cream (equivalent to the amount used in the subsequent in vivo fluorescence imaging and phototherapy assay) was applied to the skin at the tumor site of the A375 tumor-bearing mice. The absorption process was continually monitored (**Figure 4a**). Evidently, the **LipoRu** cream was completely absorbed within a duration of 5 min. To confirm the transdermal capability of **Ru2** liposomes, the distribution of **Ru2** on the surface of the nude mouse skin and at different depths after applying the cream was studied using CLSM imaging. **Ru2**

was distributed throughout various depths of the skin, especially in the hair follicles (Figure 4b,c), indicating a possibility of cream absorption through the hair follicles. Images of each scanned depth were presented in Figure S34 (Supporting Information).

To further investigate the transdermal mechanisms and capacities of the single-molecular complex **Ru2**, **Ru2**-encapsulating liposomes **LipoRu**, and **LipoRu** cream, in vitro Franz diffusion experiments were conducted at 37.0 ± 0.3 °C (Figure S35, Supporting Information). The thickness of nude mouse skin was measured as 0.42 mm. The amounts of **Ru2** that penetrated through the mouse skin were quantified using absorption spectroscopy of the opposite solution at different time points (Figure 4d). The skin area allowing drug permeation is a circular region with a diameter of 10.0 mm (78.5 $mm^2$). **Ru2** could diffuse into the opposite solution (PBS) through the nude mouse skin due to its hydrophobic character. The diffusion is significantly accelerated when **Ru2** is encapsulated in liposomes and further formulated into a cream (Figure 4d).

In vivo and ex vivo fluorescence imaging studies were further conducted to test the efficacy of different administration routes of **LipoRu** on the tumor and distribution to other organs of tumor-bearing nude mice. As shown by fluorescence imaging for living mice (**Figure** 5a) and collected organs (Figure 5b), intratumoral injection achieved an immediate high accumulation of **LipoRu** in the tumor. However, **LipoRu** concentrated at the injection site and did not spread uniformly throughout the tumor. For more accurate quantification, in addition to the fluorescence intensity data provided by live imaging (Figure 5c), ICPMS was used to analyze the content of ruthenium in the whole organ (Figure 5d,e). The liver and kidneys received a minor portion of **LipoRu** in 1 h and nearly eliminated it in 48 h. The peak accumulation of **LipoRu** in the tumor was observed at 1 h after tail vein injection. A greater amount of **LipoRu** accumulated in the liver and kidneys and remained present at 48 h. This indicates that although the EPR effect played a role, there were still challenges in achieving selective accumulation in the tumor. Remarkably, **LipoRu** administered via transdermal cream exhibited similar tumor accumulation as the intravenous injection. Nevertheless, the accumulation in the liver and kidneys was significantly decreased in comparison to intravenous injection, and it is comparable to or even lower than intratumoral injection. Applying the cream topically facilitated preferential absorption by the nearby subcutaneous tumors, despite the limited ability of **LipoRu** to reach the bloodstream through blood vessel walls. The pathway for the absorbed **LipoRu** by the skin to enter the bloodstream may involve the subcutaneous tissue and microvascular networks.

As **LipoRu** is supposed to enter the bloodstream by transdermal delivery, the fate of **Ru2** in blood circulation and further digestion behavior have also been evaluated. The urine and whole blood of the mice in in vivo fluorescence imaging studies were collected, diluted with methanol (1:10 for the urine and 1:500 for the whole blood), filtered through a 0.22 µm microporous membrane, and analyzed by HRMS-ESI to detect the possible Ru species. As the amounts of administrated **LipoRu** are quite low and the dilution of urine and blood samples are unavoidable, Ru species were detected in only one set of samples and identified as **Ru2** (Figure S36, Supporting Information). This indicates that **Ru2** did not undergo chemical reactions during circulation in the body but was excreted intact in the form of the **Ru2** complex through urine. This finding aligns with the only very early report on the in vivo metabolism of Ru complexes.[28]

In vivo phototherapy assays were conducted using the same three administration methods (**Figure** 6a) in the BALB/c mouse model with A375 tumor xenografts, based on the successful transdermal delivery of **LipoRu** cream to tumors and the distinct tumor accumulation patterns with various administration methods. The tumor-bearing mice of drug groups were administrated **LipoRu** or **LipoRu** cream. The irradiation with an 808 nm laser (100 mW $cm^{-2}$, light dose = 30.0 J $cm^{-2}$) was performed 1 h after administration to ensure an adequate absorption or accumulation of **LipoRu** in the tumors, as confirmed by the in vivo imaging assay. The efficacy of PTT was assessed by monitoring the real-time changes in the body temperature of mice using IR thermal images. In the PBS, **LipoRu** (i.t.), **LipoRu** (i.v.), and **LipoRu** cream (td) groups, the temperature of the tumor sites increased by ΔT = 4.6, 15.3, 19.5, and 22.4 °C, respectively, following exposure to 808 nm irradiation (Figure 6b). When tumor tissues are exposed to temperatures exceeding 50 °C for less than 10 min, rapid irreversible cell death can result in vessel formation and protein destruction.[8a] No skin irritation or injury was observed during the phototherapy, unlike previous studies that employed high-power lasers or xenon lamps.

At the end of the experiment (17 d after phototherapy), the survival rate of mice was 100%. In the PBS and dark groups, the tumor mean volume (V) exceeded 1300 $mm^3$ (Figure 6c; Figure S37, Supporting Information), and no decline in body weight was observed in the mice (Figure 6d). This suggests that the in vivo systemic toxicity of **LipoRu** is extremely low. The **LipoRu**+IR groups (Groups IV and VI) exhibited a notable antitumor effect. The results of in vivo phototherapy demonstrate that **LipoRu** cream applied by transdermal delivery achieved similarly effective therapeutic outcomes in comparison to intravenous injection and slightly better than intratumoral injection. Compared to injection methods, the non-invasive administration route offers advantages in terms of convenience and a milder treatment experience for patients. The variations in the hematoxylin and eosin (H&E) staining pattern of the tumor sections between the **LipoRu**+IR groups and the other groups suggested that **LipoRu**-mediated therapy could partially eradicate tumor tissues (Figure S38, Supporting Information). Moreover, the absence of any substantial lesions in the main organs serves as confirmation that the systemic toxicity of **LipoRu** in vivo is negligible. The superior therapeutic effects observed in experiments with small tumor-bearing mice still require further validation to determine applicability across other animals or humans.

The toxic effects of heavy metals on the human body, particularly on the liver and kidneys, pose a serious safety risk. The amounts of residual metals in the tumors and organs of **LipoRu**-treated mice were determined using ICP-MS at the end of the experiment (Figure 6e). Metal was found in trace amounts only in livers, kidneys, and tumors. The intravenous injection groups showed a modest increase in liver retention, while the intratumoral injection groups exhibited a higher retention in tumors. The transdermal administration groups demonstrated balanced and effective clearance. The **LipoRu** cream groups showed an average residue of 0.3%. The metals were eliminated from the body of A375 mice at higher rates than cisplatin ($t_{1/2}$ = 58–73 h), Photofrin II ($t_{1/2}$ > 100 h), and Porfimer Sodium ($t_{1/2}$ = 250 h)

 

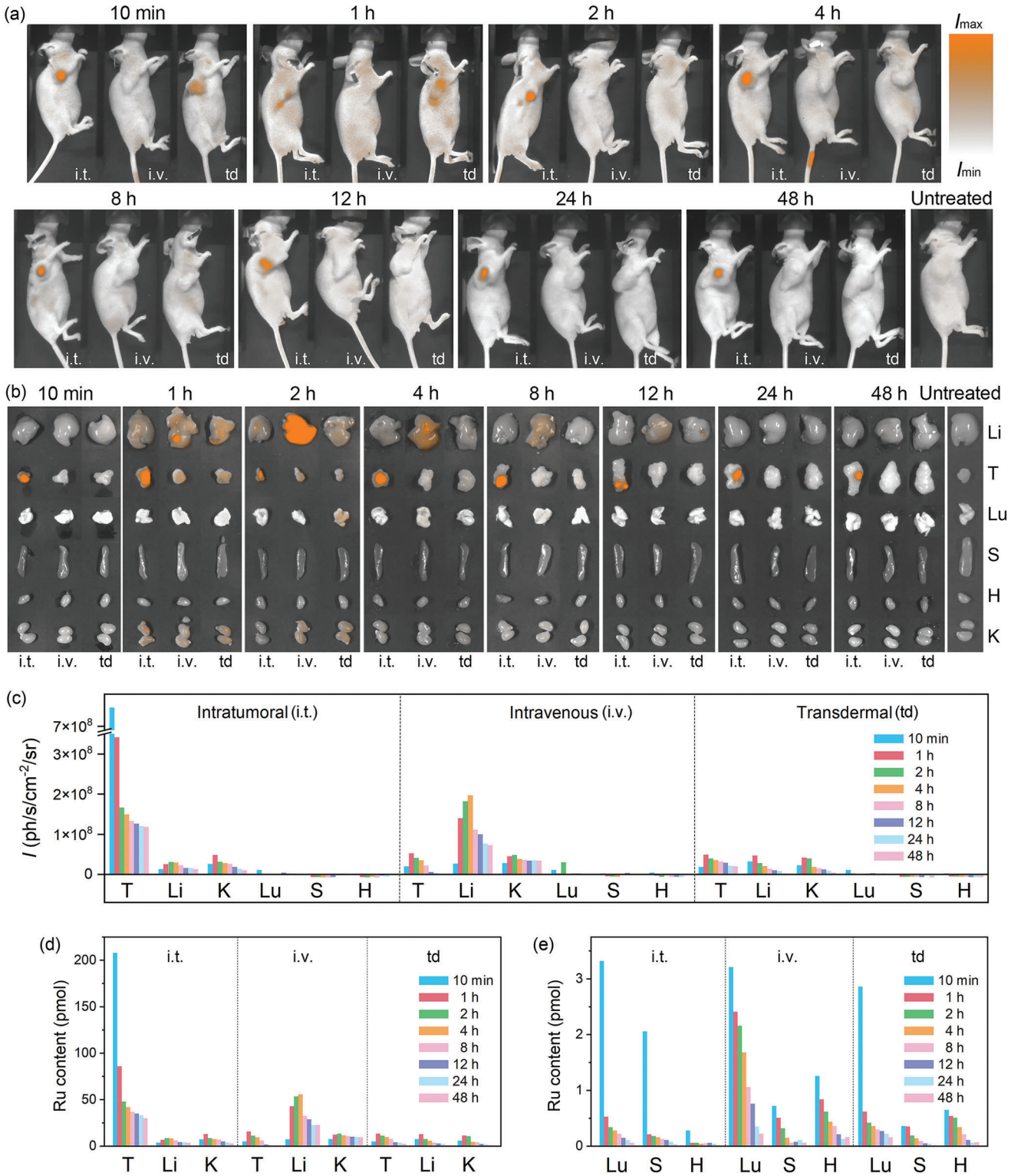


**Figure 5.** a) In vivo fluorescence imaging detection of the distribution of **LipoRu** over time in A375 tumor-bearing mice with three different administration methods: intratumoral injection (i.t.), tail intravenous injection (i.v.), and transdermal delivery (td) by topical cream application. Mouse without **LipoRu** treatment was tested as blank. Detection of the time-dependent distribution of **LipoRu** with different administration methods based on b) fluorescence imaging and c) numerical radiant flux per unit area of dissected tumors and major organs, including the liver (Li), tumor (T), lung (Lu), spleen (S), heart (H), and kidneys (K). Ru content in each examined organ (d,e) by ICPMS.

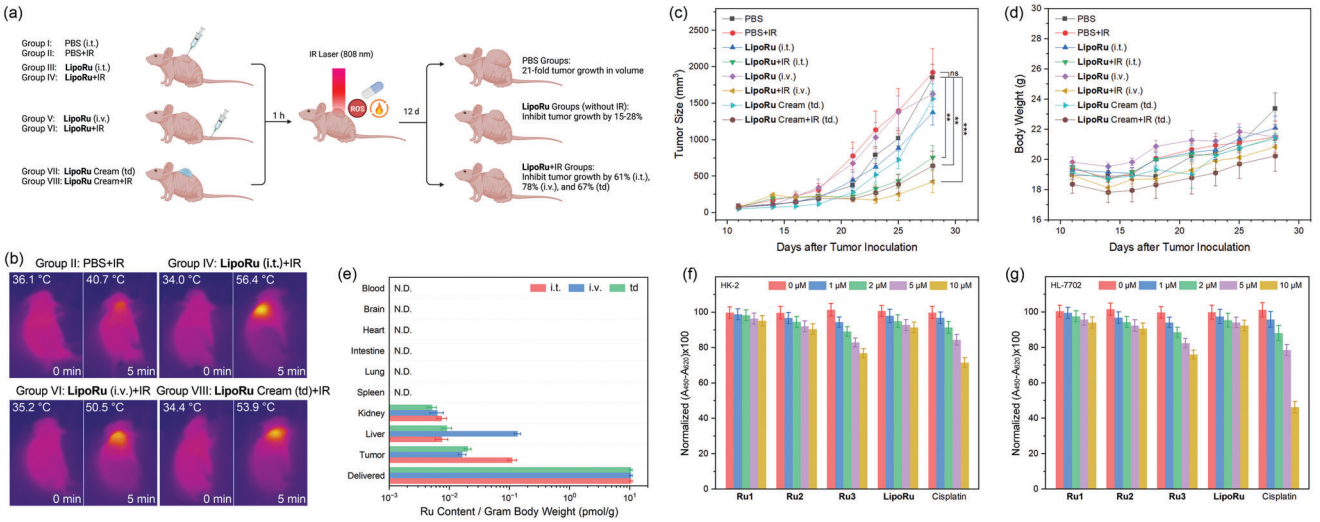


**Figure 6.** In vivo multimodal therapy of **LipoRu** toward subcutaneous A375 human melanoma xenograft model BALB/c nude mice. a) Diagram of process and summary results of in vivo assays (8 groups). b) Real-time thermal images of mice and tumors during the in vivo phototherapy. c) Histogram of mean tumor sizes for A375 tumor-bearing mice in Group I–VIII (mean ± SD, n = 4). The significance difference between two groups was assessed by one-way ANOVA test using OriginPro 2024 software. P<0.05 was the accepted level of significance ($^{**}p < 0.01$, $^{***}p < 0.001$). d) Histogram of mean body weights for A375 tumor-bearing mice in Group I–VIII (n = 4). e) Ruthenium contents in the collected organs from **LipoRu**-treated A375 tumor groups (mean ± SD, n = 8). N.D.: not detected. The amount of ruthenium delivered was calculated by the mean values of total body weight. Normalized $A_{450}-A_{620}$ (× 100) in CCK-8 assay of f) human normal kidney cell line HK-2 and g) normal liver cell line HL-7702 incubated with various doses of **Ru1–3**, **LipoRu**, and cisplatin for 24 h ([drug] = 0–10 μM, mean ± SD, n = 3).

based on the respective half-lives ($t_{1/2}$) of 46 h, 50 h, and 23 h for the **LipoRu** (i.t.), **LipoRu** (i.v.), and **LipoRu** cream (td) groups. The rapid elimination rates of **LipoRu** can not only reduce the level of metal residue, thereby enhancing safety, but also greatly decrease the occurrence of adverse effects in phototherapy, such as photodermatosis.

To evaluate the potential hepatotoxic and nephrotoxic effects of the residue of the Ru(II) complex, a study was undertaken to assess the toxicity of **Ru1–3** and **LipoRu** on normal human liver (HL-7702) and kidney (HK-2) cells. The in vitro cytotoxicity studies indicated that **Ru1–3** and **LipoRu** had minimal cytotoxic effects on both cells when not exposed to irradiation (Figure 6f,g). **Ru1–3** and **LipoRu** displayed ignorable toxicity in a range from 1 to 10 μM, which is approximately five orders of magnitude higher than the total residue of **LipoRu** found in mice. In contrast, cisplatin exhibited a significant toxicity toward HK-2 and HL-7702 cells. These results allow **LipoRu** to achieve a minimal risk level before its complete elimination from the organism.

## 3. Conclusion

In summary, we have integrated two innovative solutions: liposome-encapsulated antitumor therapeutic agents and a non-invasive and painless transdermal drug delivery cream. Initially, we developed a series of Ru(II) complexes that exhibited synergistic antitumor effects through two-photon-excited PDT, PTT, and chemotherapy. Subsequently, the selected complex **Ru2** was encapsulated into liposomes (**LipoRu**) without solid particles and formulated into a topical cream using hydrogel. The biodistribution and therapeutic efficacy of **LipoRu** in vivo have been systematically compared via three distinct administration routes: intratumoral injection, intravenous injection, and transdermal delivery through topical cream application. The positive therapeutic effects of the **LipoRu** cream fabricated here in subcutaneous tumor-bearing mice offer optimistic potential for the painless and non-invasive treatment of both early-stage and advanced skin cancers, as well as superficially located solid tumors.

## 4. Experimental Section

*Animal Ethics Statement*: Animal experiments for A375 tumor were reviewed and approved by the Institutional Animal Care and Use Committee (IACUC) at Yunnan University, Kunming, China (Approval No: YNU20240963). Dr. Xiaoxia Ren (Laboratory Animal Certificate 1118062800091) at Animal Research and Resource Center (accreditation number SYXK (滇) K2021-0002), Yunnan University, Kunming, China, performed the experiments and collected the data.

*Statistical Analysis*: The significance difference between two groups was assessed by one-way ANOVA test using OriginPro 2024 software. $p < 0.05$ was the accepted level of significance ($^{**}p < 0.01$, $^{***}p < 0.001$). Data for cytotoxicity was presented in mean ± SD (n = 3). Data for in vivo therapy was presented in mean ± SD (n = 4).

## Supporting Information

Supporting Information is available from the Wiley Online Library or from the author.

## Acknowledgements

This work was supported by the National Natural Science Foundation of China (22467023 and 22167022), the Yunnan Provincial Science and Technology Department (202401AS070139 and 202401AT070468), and the Youth Talents Project of Yunnan Province (YNWR-QNBJ-2018-057). Figure 1 is created with BioRender.com.

## Conflict of Interest

The authors declare no conflict of interest.

## Data Availability Statement

The data that support the findings of this study are available from the corresponding author upon reasonable request.

## Keywords

antitumor cream, hydrogel, lipid nanoparticle, phototherapy, skin cancer, transdermal

Received: September 18, 2024
Revised: November 15, 2024
Published online: November 21, 2024

[1] R. l. Siegel, A. N. Giaquinto, A. Jemal, *Ca Cancer J Clin.* **2024**, *74*, 12.
[2] SEER Cancer Stat Facts: Melanoma of the Skin, National Cancer Institute, Bethesda, MD.
[3] a) P. Volety, C. A. Shirley, G. Chhabra, N. Ahmad, *Photochem. Photobiol.* **2024**, *100*, 910; b) Z. Xu, M. Xu, X. Wu, S. Guo, Z. Tian, D. Zhu, J. Yang, J. Fu, X. Li, G. Song, Z. Liu, X. Song, *ChemMedChem* **2023**, *18*, 202300131.
[4] a) B. Kar, U. Das, N. Roy, P. Paira, *Coord. Chem. Rev.* **2023**, *474*, 214860; b) N.-L. Pan, J.-X. Liao, M.-Y. Huang, Y.-Q. Zhang, J.-X. Chen, Z.-W. Zhang, Z.-X. Yang, X.-E. Long, X.-T. Wu, J. Sun, *J. Inorg. Biochem.* **2022**, *229*, 111729; c) M. Ankathatti Munegowda, A. Manalac, M. Weersink, S. A. McFarland, L. Lilge, *Coord. Chem. Rev.* **2022**, *470*, 214712; d) L. Zhang, N. Montesdeoca, J. Karges, H. Xiao, *Angew. Chem., Int. Ed.* **2023**, *62*, e202300662; e) J. Karges, *Angew. Chem., Int. Ed.* **2022**, *61*, e202112236; f) C. C. James, B. de Bruin, J. N. H. Reek, *Angew. Chem., Int. Ed.* **2023**, *62*, e202306645; g) C. Queffélec, P. B. Pati, Y. Pellegrin, *Chem. Rev.* **2024**, *124*, 6700; h) F. Gao, X. Chen, J.-Q. Wang, Y. Chen, H. Chao, L.-N. Ji, *Inorg. Chem.* **2009**, *48*, 5599.
[5] a) A. Kastner, H. Schueffl, P. A. Yassemipour, B. K. Keppler, P. Heffeter, C. R. Kowol, *Angew. Chem., Int. Ed.* **2023**, *62*, e202311468; b) A. Kastner, T. Mendrina, T. Babu, S. Karmakar, I. Poetsch, W. Berger, B. K. Keppler, D. Gibson, P. Heffeter, C. R. Kowol, *Inorg. Chem. Front.* **2024**, *11*, 534; c) Y. Li, W. Lin, *Curr. Opin. Chem. Biol.* **2023**, *74*, 102290; d) Z. Deng, G. Zhu, *Curr. Opin. Chem. Biol.* **2023**, *74*, 102303.
[6] a) S. Sen, M. Won, M. S. Levine, Y. Noh, A. C. Sedgwick, J. S. Kim, J. L. Sessler, J. F. Arambula, *Chem. Soc. Rev.* **2022**, *51*, 1212; b) M. D. Pozza, P. Mesdom, A. Abdullrahman, T. D. Prieto Otoya, P. Arnoux, C. Frochot, G. Niogret, B. Saubaméa, P. Burckel, J. P. Hall, M. Hollenstein, C. J. Cardin, G. Gasser, *Inorg. Chem.* **2023**, *62*, 18510; c) Y.-Y. Liu, H.-J. Yu, Y.-P. Wang, C.-J. Li, X.-F. Wang, C.-G. Ye, H.-L. Yao, M. Pan, C.-Y. Su, *Mater. Chem. Front.* **2022**, *6*, 948; d) S. Monro, K. L. Colon, H. M. Yin, J. Roque, P. Konda, S. Gujar, R. P. Thummel, L. Lilge, C. G. Cameron, S. A. McFarland, *Chem. Rev.* **2019**, *119*, 797.
[7] a) B. M. Vickerman, E. M. Zywot, T. K. Tarrant, D. S. Lawrence, *Nat. Rev. Chem.* **2021**, *5*, 816; b) Z. Xu, Y. Yu, J. Zhao, Z. Liao, Y. Sun, S. Cheng, S. Gou, *Inorg. Chem.* **2022**, *61*, 20346; c) C. Zhang, X. Hu, L. Jin, L. Lin, H. Lin, Z. Yang, W. Huang, *Adv. Healthcare Mater.* **2023**, *12*, 2300530; d) H. Wu, L. Wang, Y. Wang, Y. Shao, G. Li, K. Shao, E. U. Akkaya, *Angew. Chem., Int. Ed.* **2022**, *61*, e202210249; e) P. Tao, Z. Lv, X.-K. Zheng, H. Jiang, S. Liu, H. Wang, W.-Y. Wong, Q. Zhao, *Inorg. Chem.* **2022**, *61*, 17703.
[8] a) X. Li, J. F. Lovell, J. Yoon, X. Chen, *Nat. Rev. Clin. Oncol.* **2020**, *17*, 657; b) Y. Ding, R. Huang, L. Luo, W. Guo, C. Zhu, X.-C. Shen, *Inorg. Chem. Front.* **2021**, *8*, 636; c) C. Xu, K. Y. Pu, *Chem. Soc. Rev.* **2021**, *50*, 1111; d) S.-J. Tang, Q.-F. Li, M.-F. Wang, R. Yang, L.-Z. Zeng, X.-L. Li, R.-D. Wang, H. Zhang, X. Ren, D. Zhang, F. Gao, *Adv. Healthcare Mater.* **2023**, *12*, 2301227; e) Y.-A. Deng, S.-J. Tang, M.-F. Wang, X. Ren, X.-L. Li, L.-Z. Zeng, D.-N. Ren, M.-R. Wang, W.-L. Xiao, Z.-Y. Cai, D. Zhang, H. Zhang, F. Gao, *Inorg. Chem. Front.* **2023**, *10*, 4552; f) M.-F. Wang, R. Yang, S.-J. Tang, Y.-A. Deng, G.-K. Li, D. Zhang, D. Chen, X. Ren, F. Gao, *Angew. Chem., Int. Ed.* **2022**, *61*, e202208721; g) S.-J. Tang, M.-F. Wang, R. Yang, M. Liu, Q.-F. Li, F. Gao, *Inorg. Chem.* **2023**, *62*, 8210; h) X.-L. Li, L.-Z. Zeng, R. Yang, X.-D. Bi, Y. Zhang, R.-B. Cui, X.-X. Wu, F. Gao, *Inorg. Chem.* **2023**, *62*, 16122; i) M.-F. Wang, Y.-A. Deng, Q.-F. Li, S.-J. Tang, R. Yang, R.-Y. Zhao, F.-D. Liu, X. Ren, D. Zhang, F. Gao, *Chem. Commun.* **2022**, *58*, 12676; j) J. Yan, H. Yu, C. Liu, B. Li, D. Wei, B. He, H. Liu, Y. Liang, Y. Sun, F. Ju, *Chem. Eng. J.* **2024**, *481*, 148616.
[9] a) Y. Yu, L. Zhang, Z. Qin, J. Karges, H. Xiao, X. Su, *Adv. Funct. Mater.* **2023**, *33*, 2208797; b) K. Xiong, C. Ouyang, J. Liu, J. Karges, X. Lin, X. Chen, Y. Chen, J. Wan, L. Ji, H. Chao, *Angew. Chem., Int. Ed.* **2022**, *61*, e202204866; c) D. Wei, Y. Huang, B. Wang, L. Ma, J. Karges, H. Xiao, *Angew. Chem., Int. Ed.* **2022**, *61*, e202201486; d) L. Wang, J. Karges, F. Wei, L. Xie, Z. Chen, G. Gasser, L. Ji, H. Chao, *Chem. Sci.* **2023**, *14*, 1461; e) H. Madec, F. Figueiredo, K. Cariou, S. Roland, M. Sollogoub, G. Gasser, *Chem. Sci.* **2023**, *14*, 409; f) L. Gourdon, K. Cariou, G. Gasser, *Chem. Soc. Rev.* **2022**, *51*, 1167; g) M.-M. Wang, F.-J. Xu, Y. Su, Y. Geng, X.-T. Qian, X.-L. Xue, Y.-Q. Kong, Z.-H. Yu, H.-K. Liu, Z. Su, *Angew. Chem., Int. Ed.* **2022**, *61*, e202203843; h) L. C.-C. Lee, K. K.-W. Lo, *J. Am. Chem. Soc.* **2022**, *144*, 14420; i) M. Tan, X. Li, H. Zhang, M. Zheng, J. Xiong, Y. Cao, G. Cao, Z. Wang, H. Ran, *Adv. Healthcare Mater.* **2023**, *12*, 2202943; j) H. Ge, J. Du, S. Long, X. Xia, J. Zheng, N. Xu, Q. Yao, J. Fan, X. Peng, *Adv. Healthcare Mater.* **2022**, *11*, 2101449; k) A. Kastner, T. Mendrina, F. Bachmann, W. Berger, B. K. Keppler, P. Heffeter, C. R. Kowol, *Inorg. Chem. Front.* **2023**, *10*, 4126; l) X. Hu, H. Li, R. Li, S. Qiang, M. Chen, S. Shi, C. Dong, *Adv. Healthcare Mater.* **2023**, *12*, 2202245.
[10] a) Y. Liu, H. Zhao, L. Li, B. Yang, Y. Yue, M. Li, X. Shi, B. Zhang, L. Wang, C. Qi, Y. Liu, S. Ren, K. Zhang, J. Yoon, *Sensor Actuat. B-Chem.* **2023**, *374*, 132836; b) S. Gao, F. Wei, J. Karges, Y. Zhao, L. Ji, H. Chao, *Inorg. Chem. Front.* **2023**, *10*, 2716; c) Z. Chen, T. Feng, J. Shen, J. Karges, C. Jin, Y. Zhao, L. Ji, H. Chao, *Inorg. Chem. Front.* **2022**, *9*, 3034; d) G. Vigueras, L. Markova, V. Novohradsky, A. Marco, N. Cutillas, H. Kostrhunova, J. Kasparkova, J. Ruiz, V. Brabec, *Inorg. Chem. Front.* **2021**, *8*, 4696; e) Z. Zheng, H. X. Liu, S. D. Zhai, H. K. Zhang, G. G. Shan, R. T. K. Kwok, C. Ma, H. H. Y. Sung, I. D. Williams, J. W. Y. Lam, K. S. Wong, X. L. Hu, B. Tang, *Chem. Sci.* **2020**, *11*, 2494; f) A. Raza, S. A. Archer, S. D. Fairbanks, K. L. Smitten, S. W. Botchway, J. A. Thomas, S. MacNeil, J. W. Haycock, *J. Am. Chem. Soc.* **2020**, *142*, 4639; g) X.-D. Bi, R. Yang, Y.-C. Zhou, D. Chen, G.-K. Li, Y.-X. Guo, M.-F. Wang, D. Liu, F. Gao, *Inorg. Chem.* **2020**, *59*, 14920.
[11] Z. Wang, L. Li, W. Wang, R. Wang, G. Li, H. Bian, D. Zhu, M. R. Bryce, *Dalton Trans.* **2023**, *52*, 1595.
[12] X. Cheng, J. Gao, Y. Ding, Y. Lu, Q. Wei, D. Cui, J. Fan, X. Li, E. Zhu, Y. Lu, Q. Wu, L. Li, W. Huang, *Adv. Sci.* **2021**, *8*, 2100876.
[13] a) E. Kong, J. Zhu, W. Wu, H. Ren, X. Jiao, H. Wang, Z. Zhang, *J. Cancer* **2019**, *10*, 2194; b) G. Qing, N. Skuli, P. A. Mayes, B. Pawel, D. Martinez, J. M. Maris, M. C. Simon, *Cancer Res.* **2010**, *70*, 10351; c) K. M. Cabanillas Stanchi, G. Bruchelt, R. Handgretinger, U. Holzer, *Cancer Biol. Ther.* **2015**, *16*, 1353.
[14] a) E. S. Kim, S. J. Keam, *Clin. Drug. Invest.* **2021**, *41*, 741; b) J. F. Hipp, F. Knoflach, R. Comley, T. M. Ballard, M. Honer, G. Trube, R. Gasser, E. Prinssen, T. L. Wallace, A. Rothfuss, H. Knust, S. Lennon-Chrimes, M. Derks, D. Bentley, L. Squassante, S. Nave, J. Nöldeke, C. Wandel, A. W. Thomas, M.-C. Hernandez, *Sci. Rep.* **2021**, *11*, 7700; c) A. Regueiro-Ren, I. B. Dicker, U. Hanumegowda, N. A. Meanwell, *ACS Med. Chem. Lett.* **2019**, *10*, 287.

[15] X.-L. Li, M.-F. Wang, L.-Z. Zeng, G.-K. Li, R.-Y. Zhao, F.-D. Liu, Y. Li, Y.-F. Yan, Q. Liu, Z. Li, H. Zhang, X. Ren, F. Gao, *Angew. Chem., Int. Ed.* **2024**, *63*, e202402028.
[16] F. E. Lytle, D. M. Hercules, *J. Am. Chem. Soc.* **1969**, *91*, 253.
[17] G. Shi, S. Monro, R. Hennigar, J. Colpitts, J. Fong, K. Kasimova, H. Yin, R. DeCoste, C. Spencer, L. Chamberlain, A. Mandel, L. Lilge, S. A. McFarland, *Coord. Chem. Rev.* **2015**, *282–283*, 127.
[18] a) E. Baggaley, M. R. Gill, N. H. Green, D. Turton, I. V. Sazanovich, S. W. Botchway, C. Smythe, J. W. Haycock, J. A. Weinstein, J. A. Thomas, *Angew. Chem., Int. Ed.* **2014**, *53*, 3367; b) J. Shen, X. Liao, W. Wu, T. Feng, J. Karges, M. Lin, H. Luo, Y. Chen, H. Chao, *Inorg. Chem. Front.* **2022**, *9*, 4171; c) G. Han, G. Li, J. Huang, C. Han, C. Turro, Y. Sun, *Nat. Commun.* **2022**, *13*, 2288; d) S. Pascal, S. David, C. Andraud, O. Maury, *Chem. Soc. Rev.* **2021**, *50*, 6613.
[19] a) Q. Feng, Z. Bennett, A. Grichuk, R. Pantoja, T. Huang, B. Faubert, G. Huang, M. Chen, R. J. DeBerardinis, B. D. Sumer, J. Gao, *Nat. Biomed. Eng* **2024**; b) M. Tang, B. Chen, H. Xia, M. Pan, R. Zhao, J. Zhou, Q. Yin, F. Wan, Y. Yan, C. Fu, L. Zhong, Q. Zhang, Y. Wang, *Nat. Commun.* **2023**, *14*, 5888; c) L. Feng, Z. Dong, D. Tao, Y. Zhang, Z. Liu, *Natl. Sci. Rev.* **2018**, *5*, 269.
[20] a) F. Wang, Z. Yuan, P. McMullen, R. Li, J. Zheng, Y. Xu, M. Xu, Q. He, B. Li, H. Chen, *Chem. Mater.* **2019**, *31*, 3948; b) H.-J. Yoon, H.-S. Lee, J.-Y. Lim, J.-H. Park, *ACS Appl. Mater. Interfaces* **2017**, *9*, 5683.
[21] a) S. Ghosh, K. A. Carter, J. F. Lovell, *Biomaterials* **2019**, *218*, 119341; b) W. Chen, E. M. Goldys, W. Deng, *Prog. Lipid Res.* **2020**, *79*, 101052.
[22] V. P. Torchilin, *Nat. Rev. Drug Discovery* **2005**, *4*, 145.
[23] Z. Liu, J. Li, D. Kong, M. Tian, Y. Zhao, Z. Xu, W. Gao, Y. Zhou, *Eur. J. Inorg. Chem.* **2019**, *2019*, 287.
[24] a) H. Liu, F. Qian, *Theranostics* **2022**, *12*, 1321; b) V. Jayashankar, A. L. Edinger, *Nat. Commun.* **2020**, *11*, 1121.
[25] a) G.-L. Ma, X.-D. Bi, F. Gao, Z. Feng, D.-C. Zhao, F.-J. Lin, R. Yan, D. Liu, P. Liu, J. Chen, H. Zhang, *J. Inorg. Biochem.* **2018**, *185*, 1; b) X. Chen, F. Gao, W.-Y. Yang, Z.-X. Zhou, J.-Q. Lin, L.-N. Ji, *Chem. Biodiver.* **2013**, *10*, 367; c) J. Sun, S. Wu, H.-Y. Chen, F. Gao, J. Liu, L.-N. Ji, Z.-W. Mao, *Polyhedron* **2011**, *30*, 1953; d) X. Chen, F. Gao, W.-Y. Yang, J. Sun, Z.-X. Zhou, L.-N. Ji, *Inorg. Chim. Acta* **2011**, *378*, 140; e) X. Chen, F. Gao, Z.-X. Zhou, W.-Y. Yang, L.-T. Guo, L.-N. Ji, *J. Inorg. Biochem.* **2010**, *104*, 576; f) F. Gao, H. Chao, F. Zhou, X. Chen, Y.-F. Wei, L.-N. Ji, *J. Inorg. Biochem.* **2008**, *102*, 1050; g) F. Gao, H. Chao, L.-N. Ji, *Chem. Biodiver.* **2008**, *5*, 1962; h) F. Gao, H. Chao, J.-Q. Wang, Y.-X. Yuan, B. Sun, Y.-F. Wei, B. Peng, L.-N. Ji, *J. Biol. Inorg. Chem.* **2007**, *12*, 1015.
[26] Y. Chen, H. Xiang, S. Zhuang, Y. Shen, Y. Chen, J. Zhang, *Adv. Mater.* **2021**, *33*, 2100129.
[27] T.-C. Chou, *Cancer Res.* **2010**, *70*, 440.
[28] J. H. Koch, W. P. Rogers, F. P. Dwyer, E. C. Gyarfas, *Aust. J. Biol. Sci.* **1957**, *10*, 342.